Published in final edited form as:
Ultrasound Med Biol. 2012 January ; 38(1): 50–61. doi:10.1016/j.ultrasmedbio.2011.10.002.

Acoustic Radiation Force Impulse Imaging of Human Prostates: Initial *in vivo* Demonstration

Liang Zhai[a], **Thomas J. Polascik**[b], **Wen-Chi Foo**[c], **Stephen Rosenzweig**[a], **Mark L. Palmeri**[a], **John Madden**[c], and **Kathryn R. Nightingale**[a]

[a]Department of Biomedical Engineering, Duke University

[b]Division of Urology, Department of Surgery, Duke University Medical Center

[c]Department of Pathology, Duke University Medical Center

Abstract

Reliably detecting prostate cancer (PCa) has been a challenge for current imaging modalities. Acoustic radiation force impulse (ARFI) imaging is an elasticity imaging method that uses remotely generated, focused acoustic beams to probe tissue stiffness. A previous study on excised human prostates demonstrated ARFI images portray various prostatic structures and has the potential to guide prostate needle biopsy with improved sampling accuracy. The goal of this study is to demonstrate the feasibility of ARFI imaging to portray internal structures and PCa in the human prostate *in vivo*. Custom ARFI imaging sequences were designed and implemented using a modified Siemens Antares^{TM} scanner with a 3D wobbler, end-firing, trans-cavity transducer, EV9F4. 19 patients were consented and imaged immediately preceding surgical prostatectomy. Pathologies and anatomic structures were identified in histological slides by a pathologist blinded to ARFI data, and were then registered with structures found in ARFI images. The results demonstrated that when PCa is visible, it is generally apparent as bilaterally asymmetric stiff structures; benign prostatic hyperplasia (BPH) appears heterogeneous with a nodular texture; the verumontanum and ejaculatory ducts appears softer compared to surrounding tissue, which form a unique 'V' shape; and the boundary of the transitional zone (TZ) forms a stiff rim separating the TZ from the peripheral zone (PZ). These characteristic appearances of prostatic structures are consistent with those found in our previous study of prostate ARFI imaging on excised human prostates. Compared to the matched B-mode images, ARFI images, in general, portray prostate structures with higher contrast. With the end-firing transducer used for this study, ARFI depth penetration was limited to 22mm, and image contrast and resolution were decreased as compared to the previous ex vivo study due to the small transducer aperture size. Even with these limitations, this study suggests ARFI imaging holds promise for guidance of targeted prostate needle biopsy and focal therapy, as well as aiding assessment of changes during watchful waiting/ active surveillance.

Corresponding Author: Liang Zhai Addr: 1230 Shorebird Way Mountain View, Ca 94043 liang.zhai@Siemens.com Ph: (650) 694-5578.

Introduction

Prostate cancer (PCa) is the most common non-skin cancer for men in the United States. It affects one in every six men during their lifetime (Cancer facts & figures, 2011). Screening techniques for PCa including digital rectal examination (DRE) and prostate-specific antigen (PSA) testing are widely used. Despite their high sensitivity to PCa, these methods have low specificity. When suspicion of PCa arises, prostate needle biopsy is performed for diagnosis. However, reliable detection of PCa has been a challenging task using current imaging modalities. Although prostate needle biopsy is typically performed with the guidance of transrectal ultrasound (TRUS), PCa, in general, does not have a unique characteristic appearance in B-mode images, which leads to random or systematic sampling of 6 – 12 biopsy cores in the prostate without targeting suspicious regions (Heidenreich et al, 2008; Lan et al, 2007; Patel and Richards, 2002). With only a small amount of prostatic tissue obtained in each biopsy core, the sampling error is high. In more than one million prostate biopsies performed each year, only about 25% of tests are positive for cancer; and the false negative rates range from 25–45% in the first time biopsy(Svetec et al, 1998; Levine et al, 1998; Roehl et al, 2002).

Extensive studies of new imaging techniques are under investigation to increase PCa's visibility. Magnetic resonance imaging (MRI) techniques including MR T2-weighted imaging, MR spectroscopy and dynamic contrast enhanced MRI have been assessed to detect PCa and guide needle biopsy, with variable results (Ahmed et al, 2009). However, high costs and availability of an endorectal coil will likely limit the wide-spread use of MRI for prostate biopsy. Color Doppler and contrast-enhanced ultrasound imaging have been reported with improved performance over conventional ultrasound, yet can be limited by their high rates of false positive findings (Cheng S, 2001; Kravchick et al, 2003; Frauscher et al, 1998, 2002; Sedelaar et al, 2001; Albrecht et al, 2000; Halpern et al, 2000, 2001). Ultrasonic tissue characterization methods have been proposed to extract the characteristic scatter signals of PCa, and are showing promise (Scheipers et al, 2008; Mohamed and Salama, 2008; Moradi et al, 2006; Feleppa et al, 2004). Based on the fact that PCa has increased stiffness, elasticity imaging techniques have been developed to differentiate cancerous regions (Parker et al, 1993; Konig et al, 2005; Tsutsumi et al, 2007; Pallwein et al, 2008b; Salomon et al, 2008; Zhang et al, 2008; Zhai et al, 2010). Multiple groups have reported improved cancer detection rates during clinical trials of elastography-guided needle biopsy (Pesavento et al, 2000; Konig et al, 2005; Tsutsumi et al, 2007; Pallwein et al, 2008a,b; Ives et al, 2005; Kamoi et al, 2008; Sumura et al, 2007; Brock et al, 2011). Yet, challenges have also been reported in applying uniform compression over the prostate, low visibility of PCa in the basal region and inability in differentiating PCa from some benign tissues such as benign prostatic hyperplasia (BPH) and prostate stones (Kallel et al, 1999; Tsutsumi et al, 2007; Salomon et al, 2008; Pallwein et al, 2008b).

Acoustic radiation force impulse (ARFI) imaging is another type of elasticity imaging. Instead of applying compression using the imaging probe during elastography, ARFI uses focused ultrasound beams to excite tissue, and infers the relative tissue stiffness based on the resultant displacement (Nightingale et al, 2002). In an ARFI imaging study of excised prostate specimens, prostatic anatomic zones, PCa and BPH nodules were readily visible in ARFI images; the results support the hypothesis that ARFI imaging will be useful for guiding prostate needle biopsy (Zhai et al, 2010). Therefore, this study was performed to investigate the feasibility of prostate ARFI imaging *in vivo*, and to provide an initial interpretation of the structures portrayed in *in vivo* prostate ARFI images. ARFI techniques were implemented using a commercially available 3D, end-firing mechanical wobbler endocavity curvilinear array. Nineteen patients with confirmed PCa were imaged *in vivo*

prior to radical prostatectomy, and the image findings were compared with histological results. Initial in vivo, 3D- ARFI prostate images are presented in this manuscript.

Materials and Methods

ARFI imaging parameters

A modified Siemens SONOLINE Anteras^{TM} ultrasound scanner and a Siemens 3D transcavity EV9F4 end-firing transducer (Siemens Medical Solutions USA, Inc., Ultrasound Division, Issaquah, WA) were used to acquire ARFI data *in vivo*. The probe has a hemispherical shape with a diameter of 25 mm. It consists of a curvilinear array with 192 elements, operating at frequencies between 4.00 MHz and 8.89 MHz. The elevational focal depth is 30 mm (F/#5.0). A motor is integrated inside the probe that can rotate the transducer in the elevation dimension with an angular range of −45° to 45° and a minimum angular step of 0.36°. An ARFI imaging sequence is comprised of interspersed ultrasonic imaging, or tracking beams and pushing beams. The following optimized parameters for this probe were determined (Zhai, 2009) and utilized for this study. ARFI excitation pulses had a center frequency of 4.0 MHz, focal depth of 20 mm, F/# of 2.9 and duration of 100 μs. 4:1 parallel-receive beamforming techniques were used for the tracking beams to reduce acquisition time. Each 2D ARFI imaging plane consisted of 55 pushing locations, and the entire 3D volume of the prostate was acquired using 50 2D planes with 1.8 degree elevational spacing. Table 1 summarizes the parameters of the ARFI imaging sequence and 3D data acquisition settings used in this study. Total volume acquisition time was 3 minutes.

For the sequence used herein, the mechanical index (MI) of the push pulses was 1.88 for the *in situ* $MI_{.7}$ ($\alpha = 0.7 dB/cm/MHz$) and 2.64 for the $MI_{.3}$ ($\alpha = 0.3 dB/cm/MHz$). The temperature rise due to acoustic absorption was simulated using a finite element method (FEM) model (Palmeri and Nightingale, 2004) for the 3D imaging sequence, which predicted the the maximum temperature rise due to acoustic absorption to be 0.5°C, located at 0.4 mm beneath the transducer surface. In addition to acoustic absorption, another source of tissue heating during ARFI imaging is the transducer itself, which was quantified empirically with thermocouple measurements. During a single 3D data acquisition, the maximum temperature rise was measured to be 3.8°C, which is below the FDA limit of 6°C (NEMA Standards Publication/No. UD 2, 1992).

Experimental procedures

This study was approved by the institutional review board (IRB) of Duke University Medical Center. Nineteen patients expecting robotic prostatectomy were consented and imaged at Duke Medical Center. Patients were recruited from those with known PCa who had elected to have a radical prostatectomy. They were not selected specifically based upon their PSA levels, Gleason scores of biopsy results or DRE findings; patients who had been previously treated by radiation, cryoablation, chemotherapy, high intensity focused ultrasound (HIFU) and hormone therapy were excluded from the study. ARFI imaging was performed immediately before the prostatectomy after the patient was anesthetized. The patient was put in a dorsal lithotomy position as shown in Figure 1a. The relative positions between the imaging probe and the prostate are shown in Figure 1b. During imaging, the probe was held either by the physician or with a surgical transducer holder (part # 810–205, CIVCO medical solutions, Kalona, Iowa, USA). Real-time 2D ultrasound imaging was used to locate the prostate and position the imaging probe at the middle of the prostate before beginning the 3D ARFI data acquisition. Only a few 2D ARFI images were acquired in the first patient in order to test the *in vivo* imaging setup and the ARFI imaging sequence; 3D ARFI data were acquired from the remaining 18 patients.

Data analysis

ARFI data were processed off-line. ARFI displacement at 0.4 ms post-push was estimated along each lateral location using Loupas' algorithm (Pinton et al, 2006). The displacement was normalized using a depth dependent gain (DDG) algorithm to compensate for the effects of the spatial gradient in acoustic radiation force amplitudes (Zhai et al, 2010). The normalized ARFI displacement data were resampled to 0.1 mm in all three dimensions in the Cartesian coordinate system using a Delaunay triangulation method (Watson, 1994).

To facilitate registration between ARFI and histological data, prostate volumes were reconstructed from the histological slides. A custom sectioning device was used to divide the prostate specimen into parallel tissue slices every 3 mm after fixation in formalin for 48 hours (3–4 mm is the standard medical practice during pathological sectioning). Standard histological processing was performed to mount a 5-micron thick tissue sample section taken from each 3 mm slice onto microscope slides. Due to the large area of these tissue slices, each sample was further divided into halves or quarters to fit onto the microscope slides. The locations of tissue samples on all microscope slides (histological slides) were recorded to guide reconstruction of the prostate volume in later analysis. The standard haematoxylin and eosin (H&E) staining method was used for all specimens. PCa, benign prostatic hyperplasia (BPH), atrophy and anatomic landmarks (i.e. seminal vesicles (SV), ejaculatory ducts, urethra and verumontanum) were identified, and marked with red, blue, black and green ink on the histological slides respectively by a pathologist blinded to the ARFI images. A Gleason's score was assigned for each identified cancerous region.

ARFI volumes were reviewed by the authors (L. Zhai, M. Palmeri and K. Nightingale) before being compared to histological data, based upon typical appearance of structures and pathology as determined in the ex vivo study (Zhai et al, 2010), and regions suspicious for cancer were manually segmented. Stiff regions over 3 mm in their smallest dimensions, which presented bilateral asymmetry, were identified to be suspicious for cancer. Then, ARFI data were compared to the findings in histological data. Histological slides were digitized, and assembled using adobe Photoshop to form 2D whole mount sections based on the sectioning diagrams, and then were imported to ImageJ (http://rsbweb.nih.gov/ij) to reconstruct the prostate volumes. Displayed side by side using the same base-apex and left-right orientation, the orientation of ARFI and histological data was adjusted to achieve optimal registration based on prostate boundaries and key anatomic structures (i.e. urethra, verumontanum). Finally, the prostate volume was divided into six regions as shown in Figure 2. When a region that was identified as suspicious for cancer on ARFI images was determined to be in the same region as that in histological data, the lesion was considered visualized in ARFI data. To estimate the size of each lesion, the largest extent in each dimension was measured to represent the lesion size in ARFI data; in the histological data, the largest area within the planes on the histologic slides were measured. Anatomic structures such as central zone (CZ), peripheral zone (PZ), transition zone (TZ) and verumontanum were identified based upon their appearance as determined from the ex vivo study (Zhai et al, 2010).

Images were displayed with the same lateral directionality (left and right) as that in normal human anatomy (i.e. the left side of the patient's prostate is shown on the left side of the image). ARFI and logarithmically compressed B-mode images are displayed in two linear colormaps, copper and gray, respectively. The contrast-to-noise ratio (CNR) of each confirmed PCa lesion was computed using the following equation for both ARFI and B mode coronal images:

$$CNR=\frac{|S_1 - S_2|}{\sqrt{\left(\sigma_1^2+\sigma_2^2\right)/2}}, \quad (1)$$

in which S_1 and S_2 are the mean image brightness values of PCa and healthy tissue on the contra-lateral side, and σ_1 and σ_2 are the standard variations of the two areas. The lesionto-healthy-tissue stiffness ratio (SR) was computed using the inverse of the displacement amplitudes in the ARFI images as follows:

$$SR=\frac{S_2}{S_1} \quad (2)$$

In the results section, prostate images were selected from all patients; the identifiers (A, B, C…) are used to differentiate from each other, and are not in the order of data acquisition.

Results

Figure 3 shows the matched B-mode, ARFI and histological prostate images acquired from patient A. The axial view (top row) is the normal imaging plane of an end firing probe, with the probe located at the bottom of the images. Two coronal planes (row 2 and 3) which intersect the axial imaging plane at the dashed lines, A and B, are also displayed from the 3D dataset. In the coronal views, the prostate base is near the top of the images; and the apex is near the bottom of the images; regions outside the prostate were masked in black based on the prostate boundary as determined from the matched B-mode image in the coronal views. While the B-mode images show poor structural contrast, there is an obvious stiff structure in the right apex in the ARFI images that corresponds to the lower cancerous region marked with red ink in the histology image, which was reconstructed from two histological slides taken in the same plane. The size of the lesion was measured to be $12 \times 10 \times 14 mm^3$ in the ARFI volume, and $11 \times 8 mm^2$ in the histological slide. The CNR of this lesion was computed based on the two areas circled in white dotted lines to be 2.8 in the ARFI image and 0.4 in the B mode. The SR was 1.9. The Gleason's score of this lesion is 4+3. The relatively softer central structure (circled in green dashed lines) to the left of the confirmed PCa corresponds to the ejaculatory ducts and verumontanum (green arrow) identified in the histological slides. The histological image shown here intersects with the two coronal ARFI images with an estimated angle of 15°. Besides the confirmed PCa region, some bilaterally asymmetric displacement variations (yellow arrow) were identified as suspicious PCa lesions in the ARFI coronal image. However, correlation between these other stiff areas in the ARFI image and cancerous regions identified in the histological slides was not adequate to confirm a match. The horizontal stripes seen in the coronal images (−7 to 10 mm at the elevation dimension) are artifacts generated from transducer motion (caused by hand movement) between data acquisition at different imaging planes.

Figure 4 shows the matched coronal B-mode, ARFI and histological prostate images acquired from patient B. The asymmetric stiff region (indicated by the red arrow) at the left base corresponds to the cancerous area (masked in red) in the histological image. This whole-mount histological image was reconstructed from 4 different slides taken in the same plane. The PCa was measured to be $15 \times 8 \times 7 mm^3$ in the ARFI volume, and $10 \times 8 mm^2$ in the histological slide. In the coronal view, the CNRs were computed based on the areas circled in white dotted lines to be 2.5 in the ARFI data and 1.5 in the B-mode. The SR was 1.5. The Gleason's score of this PCa is 3+3. The bright region (8 mm lateral, −6 mm elevation) in the right part of the ARFI image at the intersection line corresponds to the hyperechoic calcifications shown in the B-mode image.

Figure 5 shows another set of matched B-mode, ARFI and histological prostate images acquired from Patient C. In the coronal ARFI image, the asymmetric stiff structure on the right corresponds to PCa identified in histological data (Gleason's score, 3+4). The lesion size was measured to be $8\times13\times7 mm^3$ in the ARFI volume, and $7\times11 mm^2$ in the histological slide. Based on the areas circled by the white dotted lines in the coronal view, the CNRs were computed to be 1.9 for the ARFI image, and 0.4 for the B-mode. The SR was 1.5. The central softer structure corresponds to the two ducts (ejaculatory ducts merging to the verumontanum) identified in the histological image.

Figure 6 shows the registered axial and coronal B-mode and ARFI images with a histological image from Patient D. Due to the large size of this prostate, ARFI data from only part of the prostate volume was acquired; and good registration between ARFI and histological images could not be achieved. Based on the histological analysis, this prostate had complicated BPH development; only two PCa foci (less than 0.5 mm) were found throughout the prostate histology images; and some atrophied tissue (colored black in histology) was identified around the prostate outer boundary. Based on the findings from the *ex vivo* ARFI prostate imaging study of the characteristic appearances of zonal structures (Zhai et al, 2010), the stiff region at the base (top in the coronal ARFI image) is likely to be the CZ and seminal vesicles. The middle region is likely the transitional zone (TZ) with a stiff boundary (green arrows) that is visible in the ARFI image. The axial ARFI image clearly portrays the separated TZ and PZ. Inside the TZ, the nodular texture is likely caused by the BPH structures.

Table 2 summarizes the findings from all 19 patients. One patient was recruited to test the imaging sequence; and no volume data were acquired. In 3 cases, the ARFI data were noisy due to bad coupling between the probe and the rectal wall, and could not be evaluated. In 5 cases, stiff bilateral asymmetries were seen in the acquired volume ARFI data; however, registration between ARFI and histology data was not achieved. In 7 cases (including those shown in Figures 3, 4 and 5), at least one PCa, confirmed by the registered histological data, was identified as suspicious for cancer in the ARFI data. Table 3 summarizes the sizes, CNRs, SRs and Gleason's scores of all confirmed PCa in the 7 cases. In the remaining 3 cases, including that shown in Figure 6, no focal PCa larger than 2 mm was identified in the histological analysis.

Discussion

This study is the first demonstration of the feasibility of ARFI prostate imaging *in vivo*. ARFI techniques were successfully developed on a commercially available 3D end-firing curvilinear endocavity probe using custom designed beam sequences. The experimental setting was similar to that currently used in TRUS imaging during prostate needle biopsy, thus could be conveniently adapted to guide prostate needle biopsy in further studies. Besides technical development, the other goal for this study was to provide an initial interpretation of the structures portrayed in the *in vivo* ARFI images. By registering ARFI data to histological data, characteristic appearances of various prostatic structures were identified, which were found to be similar to those determined in a previous *ex vivo* study (Zhai et al, 2010). For this purpose, the data were only reviewed by the authors. In future studies, trained and blinded data reviews will be adopted to characterize the PCa detection accuracy of ARFI imaging. In the initial data from 19 patients, anatomical structures and some prostate lesions (i.e. BPH and PCa) were readily observed in the ARFI volume data. ARFI images consistently portray more structural details and higher PCa CNRs compared to the matched B-mode ultrasound images.

Registration between histological and ARFI data was a challenging task during this study. In contrast to our previous study of prostate ARFI imaging *ex vivo*, in which ARFI and histological data could be aligned in 2D (Zhai et al, 2010), registration between ARFI and histological data had to be performed over three dimensions, due to different image acquisition orientation between in vivo and ex vivo imaging, which occurred for the following reasons. First, the position and orientation of the imaging probe were limited by the rectal cavity. The exact angle between the imaging probe and the prostate was not always known. Second, due to the limited field of view (FOV) of the imaging probe, usually only part of the prostate was acquired. Third, some compression of the prostate was applied with the transducer during imaging to achieve good acoustic coupling, which distorted the prostate shape as compared to the *ex vivo* geometry. In addition, when the prostate is fixed in formalin and sectioned for mounting on histological slides, considerable shrinking and distortion occurs. Although much effort was devoted into registering ARFI and histological data, good registration for some of the prostates was still not achieved.

Due to the nature of the wobbler imaging probe, the 2D imaging planes (lateral-axial planes) were not parallel to each other. Therefore, the 2D imaging planes were not the axial anatomic planes. Also, the probe could not be positioned perpendicular to the prostate posterior surface due to the limit imposed by the rectal space. Thus, the orthogonal imaging planes (perpendicular to the central axis of the probe) were different from the anatomic coronal planes as well. Throughout this paper, the terms, `axial' and `coronal' planes were only used to indicate regular 2D ultrasonic and the orthogonal imaging planes for convenience.

As shown in Figures 3, 4 and 5 and table 3, PCa exhibits higher contrast in ARFI images than in the matched B-mode images. This observation is consistent with that found in our previous ARFI imaging study of excised human prostates (Zhai et al, 2010). Another observation consistent with previous *ex vivo* results is that when visualized, PCa is stiffer (darker in ARFI images) than the surrounding tissue, and can introduce bilateral stiffness asymmetries, which are most clearly visualized in the coronal ARFI views. In the nine lesions shown in table 3, the PCa-Normal stiffness ratio is between 1.2 to 2.1, which is in good agreement with previous studies (Krouskop et al, 1998; Zhang et al, 2008; Zhai et al, 2010a). The stiffening effect of PCa has been demonstrated by many groups and is the physical mechanism for elasticity imaging techniques to identify PCa (Krouskop et al, 1998; Phipps, 2006; Jalkanen et al, 2006; Zhang et al, 2008; Zhai et al, 2010a). The bilateral stiffness asymmetry created by PCa in ARFI images may provide a convenient means to identify suspicious malignancy in the prostate. As suspicious regions did not have sharp boundaries in ARFI images, the `lesion sizes' reported in the table are subjective and approximate. Also, given the different orientations and tissue distortion introduced during ARFI imaging and pathological processing, exact agreement on sizes is not expected in this study. However, the ability of ARFI imaging to detect cancerous regions will be highly valuable. When ARFI imaging is used to guide prostate needle biopsy, the center of the suspicious region would be targeted, which would be expected to correlate with histology.

Figure 6 shows a case with complicated BPH development in the enlarged TZ. The stiff rim around the TZ corresponds to the fibromuscular layer between the TZ and PZ in the histology. The heterogeneous structures are likely caused by the distribution of BPH nodules. These two features are consistent with those of TZ and BPH tissue seen in the previous *ex vivo* prostate ARFI imaging study (Zhai et al, 2010). Multiple groups investigating transducer compression-based elastography of the prostate have reported that both PCa and BPH nodules appear as stiff structures, and have thus reported difficulty in differentiating between them (Pallwein et al, 2008b; Sumura et al, 2007; Salomon et al, 2008). The characteristic appearance of the zonal anatomy and the heterogeneous structure

of BPH in ARFI images may be helpful in addressing this challenge, because PCa has a much higher incidence rate in the PZ than in the other two zones combined; and BPH primarily develops in the TZ (De Marzo et al, 2007). A considerably larger sample size would be needed to assess the ability of ARFI imaging to differentiate these two types of prostate lesions. While the appearance of BPH in ARFI images differs from other elastography imaging methods, BPH presents similar textures in MR T2 weighted images and ARFI images (Oto et al, 2010).

Figure 4 shows the typical appearance of prostate calcification in the ARFI images. Regions of calcification were shown with larger displacement amplitudes as compared to the surrounding tissue, which is consistent with our findings in the previous *ex vivo* prostate ARFI imaging study (Zhai et al, 2010). This differs from the reported appearance of prostate calcifications in compression elastography, which appear to be stiffer than normal tissue, creating false positive findings during compressive elastography-based image-guided needle biopsy procedures (Lorenz et al, 1999; Jalkanen et al, 2006). The apparent disparity is likely due to two factors. First, calcifications are highly scattering of ultrasound (hyperechoic in B-mode images), which can result in larger acoustic radiation force being applied to them than the surrounding tissue. The large displacement may be primarily the response of surrounding tissue pushed by the increased acoustic radiation force, due to the distributive property of calcification particles. Second, calcifications are generally small rigid particles that develop in the fluid filled prostate glands. When pushed by acoustic radiation force, small calcified particles likely move within the fluid, thus their displacements could reflect their mobility, rather than their inherent material stiffness. Whatever the cause, this finding is advantageous for ARFI imaging in that calcifications can easily be differentiated from PCa lesions.

The verumontanum, the junction of ejaculatory ducts and urethra, appears to be a good landmark for determining the prostate orientation, and in registration of ARFI data to the histological slides. The two ejaculatory ducts form a unique soft `V' shape and merge to the verumontanum (Figures 2 and 4), which is very distinctive in ARFI images. This observation is also in agreement with the previous *ex vivo* prostate ARFI imaging study (Zhai et al, 2010).

Table 3 summarizes PCa findings in all cases with matched ARFI and histological data. The z-dimension of PCa in histological data was not measured due to distortions during histological processing and difficulty to reconstruct 3D histological volumes accurately. The prostate specimen shrinks during tissue fixation in formalin. After the prostate was sectioned into a series of tissue sections, each section expanded due to release of internal pressure. Then further distortion was introduced during subdivision of each section and mounting the tissue sample to microscope slides. Distortion was also observed during slicing. Although a custom sectioning device was designed to divide the specimen into parallel sections every 3 mm, noticeable shape change of the specimen was observed when pressing the blade against the specimen. Thus, the z-dimension of PCa measured from reconstructed histological volume could not be determined accurately.

The minimum size of PCa that can be detected in an ARFI image was not characterized in this study. Palmeri et al. has shown the lesion-to-background contrast in ARFI images to be dependent on a number of factors, such as the lesion stiffness contrast, focal configuration of the push pulses, the spatial location (axially) of the lesion, the time after push when ARFI displacement is monitored, as well as the size of the lesion (Palmeri et al, 2006). Thus, the minimum detectable lesion size will vary with the ARFI sequence parameters and lesion material properties. Also, it is likely that PCa can have a range of stiffness depending on its Gleasons grades and morphology (focal or diffused). Clinically, detection of significant PCa is desired. Therefore, further studies will be required to characterize the minimum detectable

size of PCa in ARFI images, and optimize ARFI imaging parameters to meet the clinical needs. For this initial evaluation, only suspicious areas greater than 3 mm in the smallest dimensions that can be confidently correlated with histological data were included.

Besides the common characteristics of prostatic structures demonstrated in both the previous *ex vivo* and this *in vivo* study, there are a few differences identified between these two studies. Compared to the *ex vivo* results, the *in vivo* ARFI images have lower contrast and less resolution. This effect is primarily attributed to the large curvature of the imaging transducer, which presents challenges for the generation of tightly focused acoustic beams due to limited angular sensitivity of the elements, although the focal configuration for ARFI push pulses used in this study was optimized for this imaging probe. The cross-sectional area of the push beam at the focus using the EV9F4 in this study is 8 times larger than that used in the *ex vivo* study (Zhai, 2009). With these less tightly focused push beams, lower structural contrast in ARFI images is expected (Palmeri et al, 2006). The curvature of the EV9F4 transducer also limited the achievable depth penetration for the requisite focal configuration of the pushing beams to 20 mm. Due to the limited rectal space and transducer geometry, the CZ was generally at a greater depth *in vivo* than in the *ex vivo* study, thus was often not included in the ARFI imaging FOV. These challenges will be addressed in future studies by development of a side-firing, larger aperture array with an increased elevational sweeping range.

Conclusion

This paper presents the first *in vivo* ARFI images of human prostate. Volumetric ARFI prostate data were successfully acquired in patients and reconstructed to visualize the internal prostate structures. ARFI images portray more structural detail with higher contrast than matched B-mode images. The appearances of prostatic structures seen in the *in vivo* ARFI images are consistent with those found in the previous *ex vivo* study. The appearance of PCa was consistent with that reported for compression elastography, however, BPH and calcifications appeared with more detail and different contrast in ARFI images. Along with these encouraging findings, some limitations of the current implementation, mainly due to the transducer geometry, were identified. This study suggests ARFI imaging holds promise for guidance of targeted prostate needle biopsy and focal therapy, as well as aiding assessment of changes during watchful waiting/active surveillance.

Acknowledgments

The authors would like to thank Dr. Gregg Trahey for his valuable insights in this project and Siemens Healthcare, Ultrasound Business Unit for their technical support. This work is supported by NIH 1R01 CA-114075, R01CA142824, R01EB002132 and US ARMY Prostate Cancer Research Program (W81XWH-08-1-0132).

References

Ahmed H, Kirkham A, Arya M, Illing R, Freeman A, Allen C, Emberton M. Is it time to consider a role for mri before prostate biopsy. Nature Reviews Clinical Oncology. 2009; 6:197–206.

Albrecht T, Hoffmann C, Schettler S. B-mode enhancement at phase-inversion us with air-based microbubble contrast agent: initial experience in humans. Radiology. 2000; 216:273–8. [PubMed: 10887261]

American Cancer Society. Cancer facts & figures 2011. American Cancer Society; Atlanta, Ga: 2011.

Brock M, Bodman C, Sommerer F, Loppenberg B, Klein T, Deix T, Palisaar J, Noldus J, Eggert T. Comparison of real-time elastography with grey-scale ultrasonography for detection of organ-confined prostate cancer and extra capsular extension: a prospective analysis using whole mount sections after radical prostatectomy. British Journal of Urology international. Aug 5.2011 Online.

Cheng SR. Color doppler imaging of the prostate: important adjunct to endorectal ultra-sound of the prostate in the diagnosis of prostate cancer. Ultrasound Q. 2001; 17:185–189. [PubMed: 12973076]

Marzo AD, Platz E, Sutcliffe S, Xu J, Gronberg H, Drake C, Nakai Y, Isaacs W, Nelson W. Inflammation in prostate carcinogenesis. Nature Reviews Cancer. 2007; 7:256–269.

Feleppa E, Porter C, Ketterling J, Lee P, Dasgupta S, Urban S, Kalisz A. Recent developments in tissue-type imaging (tti) for planning and monitoring treatment of prostate cancer. Ultrason Imaging. Jul; 2004 3(26):163–72. [PubMed: 15754797]

Frauscher E, Helweg G, Gotwald T. The value of contrast-enhanced color doppler ultra-sonography in the diagnosis of prostate cancer. Radiology. 1998; 209

Frauscher F, Klauser A, Volgger H. Comparison of contrast enhanced color doppler targeted biopsy with conventional systematic biopsy: impact on prostate cancer detection. J Urol. 2002; 167:1648–52. [PubMed: 11912381]

Halpern E, Rosenberg M, Gomolla L. Contrast enhanced sonography of the prostate. Radiology. 2001; 219:219–25. [PubMed: 11274560]

Halpern E, Verkh L, Forsberg F. Initial experience with contrast-enhanced sonography of the prostate. AJR. 2000; 174:1757–58.

Heidenreich A, Aus G, Bolla M, Joniau S, Matveev V, Schmid HP, Zattoni F. Eau guidelines on prostate cancer. Eur. Urol. 2008; 53:68–80. [PubMed: 17920184]

Ives, E.; Waldman, I.; Gomella, L.; Halpern, E. Preliminary experience with prostate elastography and comparison with biopsy results. 2005 Prostate Cancer Symposium; 2005.

Jalkanen V, Andersson B, Bergh A, Ljungberg B, Lindahl O. Resonance sensor measurements of stiffness variations in prostate tissue in vitro-a weighted tissue proportion model. Physiol Meas. 2006; 27(12):1373–86. [PubMed: 17135706]

Kallel F, Price R, Konofagou E, Ophir J. Elastographic imaging of the normal canine prostate in vitro. Ultrasonic Imaging. Jul; 1999 21(3):201–215. [PubMed: 10604801]

Kamoi K, Okihara K, Ochiai A, Ukimura O, Mizutani Y, Kawauchi A, Miki T. The utility of transrectal real-time elastography in the diagnosis of prostate cancer. Ultrasound Med. Biol. 2008; 34(7):1025–1032. [PubMed: 18255215]

Konig K, Scheipers U, Pesavento A, Lorenz A, Ermert H, Senge T. Initial experiences with real-time elastography guided biopsies of the prostate. J Urol. 2005; 174(1):115–117. [PubMed: 15947593]

Kravchick S, Cytron S, Peled R, Altshuler A, Ben-Dor D. Using gray-scale and two different techniques of color doppler sonography to detect prostate cancer. Urology. May; 2003 65(5):977–81. [PubMed: 12736019]

Krouskop T, Wheeler T, Kallel F, Garra B, Hall T. lastic moduli of breast and prostate tissues under compression. Ultrason Imaging. 1998; 20(4):151–159. [PubMed: 9921616]

Lan S, Tsai Y, Lin Y, Tzai T. Diagnostic performance of a random versus lesion-directed biopsy of the prostate from transrectal ultrasound: results of a 5-year consecutive clinical study in 1 institution in south taiwan. J Ultrasound Med. 2007; 26(1):11–7. [PubMed: 17182704]

Levine M, Ittman M, Melamed J, Lepor H. Two consecutive sets of transrectal ultrasound guided sextant biopsies of the prostate for the detection of prostate cancer. J Urol. 1998

Lorenz A, Sommerfeld H, Garcia-Schurmann M, Philippou S, Senge T, Ermert H. A new system for the acquisition of ultrasonic multicompression strain images of the human prostate *in vivo*. Ieee Transactions on Ultrasonics Ferroelectrics and Frequency Control. 1999; 46(5):1147–54.

Mohamed S, Salama M. Prostate cancer spectral multi-feature analysis using trus images. IEEE Trans Med Imaging. Apr; 2008 27(4):548–56. [PubMed: 18390351]

Moradi, M.; Abolmaesumi, P.; Isotalo, P.; Siemens, D.; Sauerbrei, E.; Mousavi, P. A new feature for detection of prostate cancer based on rf ultrasound echo signals. 2006 IEEE Ultrasonics Symposium; 2006. p. 2084-87.

NEMA Standards Publication/No. UD 2. Acoustic Output Measurement Standard for Diagnostic Ultrasound Equipment. National Electrical Manufacturers Association; Washington, D.C.: 1992.

Nightingale K, Bentley R, Trahey G. Observations of tissue response to acoustic radiation force: Opportunities for imaging. Ultrasonic Imaging. 2002; 24:100–108. [PubMed: 12199416]

Oto A, Kayhan A, Jiang Y, Tretiakova M, Yang C, Antic T, Dahi F, Shalhav A, Karczmar G, Stadler W. Prostate Cancer: Differentiation of Central Gland Cancer from Benign Prostatic Hyperplasia by Using Diffusion-weighted and Dynamic Contrast-enhanced. MR Imaging. 2010; 257:715–723.

Pallwein L, Aigner F, Faschingbauer R, Pallwein E, Pinggera G, Bartsch G, Schaefer G, Struve P, Frauscher F. Prostate cancer disgnosis: value of real-time elastography. Abdominal Imaging. Jan. 2008a 33:729–735. [PubMed: 18196315]

Pallwein L, Mitterberger M, Pelzer A, Bartsch G, Strasser H, Pinggera GM, Aigner F, Gradl J, Nedden Z, Frascher F. Ultrasound of prostate cancer: recent advances. Eur. Radiol. 2008b; 18:707–715. [PubMed: 17938936]

Palmeri M, McAleavey S, Fong K, Trahey G, Nightingale K. Dynamic mechanical response of elastic spherical inclusions to impulsive acoustic radiation force excitation. IEEE Trans. Ultrason., Ferroelec., Freq. Contr. 2006; 53(11):2065–2079.

Palmeri M, Nightingale K. On the thermal effects associated with radiation force imaging of soft tissue. IEEE Trans. Ultrason., Ferroelec., Freq. Contr. 2004; 51(5):551–565.

Parker, K.; Huang, S.; Lerner, R.; Lee, F.; Rubens, D.; Roach, D. Elastic and ultrasonic properties of the prostate. 1993 IEEE Ultrasonics Symposium; 1993. p. 1035-38.

Patel U, Richards D. Handbook of Transrectal Ultrasound and Biopsy of the Prostate. Informa Healthcare. 2002

Pesavento A, Lorenz A, Siebers S, Ermert H. New real-time strain imaging concepts using diagnostic ultrasound. Physics in Medicine and Biology. 2000; 45(6):1423–1435. [PubMed: 10870701]

Phipps S. Prostate tissue stiffness as measured with a resonance sensor system: a study on silicone and human prostate tissue in vitro. Med Biol Eng Comput. 2006; 44(11):941–3. [PubMed: 17061118]

Pinton G, Dahl J, Trahey G. Rapid tracking of small displacements with ultrasound. IEEE Trans. Ultrason., Ferroelec., Freq. Contr. 2006; 53(6):1103–1117.

Roehl K, Antenor J, Catalona W. Serial biopsy results in prostate cancer screening study. J Urol. 2002

Salomon G, Kollerman J, Thederan I, Chun L, Budaus L, Schlomm T, Isbarn H, Heinzer H, Huland H, Graefen M. Evaluation of prostate cancer detection with ultrasound real-time elastography: A comparison with step section pathological analysis after radical prostatectomy. European Urology. Dec; 2008 54(6):1354–1362. [PubMed: 18374470]

Scheipers U, Konig K, Sommerfeld H, Garcia-Schurmann M, Senge T, Ermert H. Sonohistology - ultrasonic tissue characterization for prostate cancer diagnostics. Cancer Biomarkers. 2008; 4(4–5):227–250. [PubMed: 18957713]

Sedelaar J, Van Leenders G, Hulsbergen-Van Dekaa C. Microvessel density: correlation between cantrast ultrasonography and histology of prostate cancer. Eur Urol. 2001; 40:285–293. [PubMed: 11684844]

Sumura M, Shigeno K, Hyuga T, Shiina H, Igawa M. Initial evaluation of prostate cancer with real-time elastography based on step-section pathologic analysis after radical prostatectomy: A preliminary study. International Journal of Urology. Sep; 2007 14(9):811–816. [PubMed: 17760747]

Svetec D, McCabe K, Peretsman S, Klein E, Levin H, Optenberg S, Thompson I. Prostate rebiopsy is a poor surrogate of treatment efficacy in localized prostate cancer. J Urol. 1998; 159(5):1606–1608. [PubMed: 9554363]

Tsutsumi M, Miyagawa T, Matsumura T, Kawazoe N, Ishikawa S, Shimokama T, Shiina T, Miyanaga N, Akaza H. The impact of real-time tissue elasticity imaging (elastography) on the detection of prostate cancer: clinicopathological analysis. The Japan Society of Clinical Oncology. 2007; 12(4):250–5.

Watson D. Contouring: A Guide to the Analysis and Display of Spatial Data. Pergamon. 1994

Zhai, L. Ph.D. thesis. Duke University; 2009. Imaging and characterizing human prostates using acoustic radiation force.

Zhai L, Madden J, Foo W, Palmeri M, Mouraviev V, Polascik T, Nightingale K. Acoustic radiation force impulse imaging of human prostate ex vivo. Ultrasound Med. Biol. 2010; 36(4):576–588. [PubMed: 20350685]

Zhang M, Nigwekar P, Castaneda B, Hoyt K, Joseph J, Agnese A, Messing E, Strang J, Rubens D, Parker K. Quantitative characterization of viscoelastic properties of human prostate correlated with histology. Ultrasound in Medicine and Biology. 2008; 34(7):1033–42. [PubMed: 18258350]

Zhai L, Madden J, Foo W, Mouraviev V, Polascik T, Palmeri M, Nightingale K. Characterizing stiffness of human prostate using acoustic radiation force. Ultrasonic imaging. 2010; 32:201–213. [PubMed: 21213566]

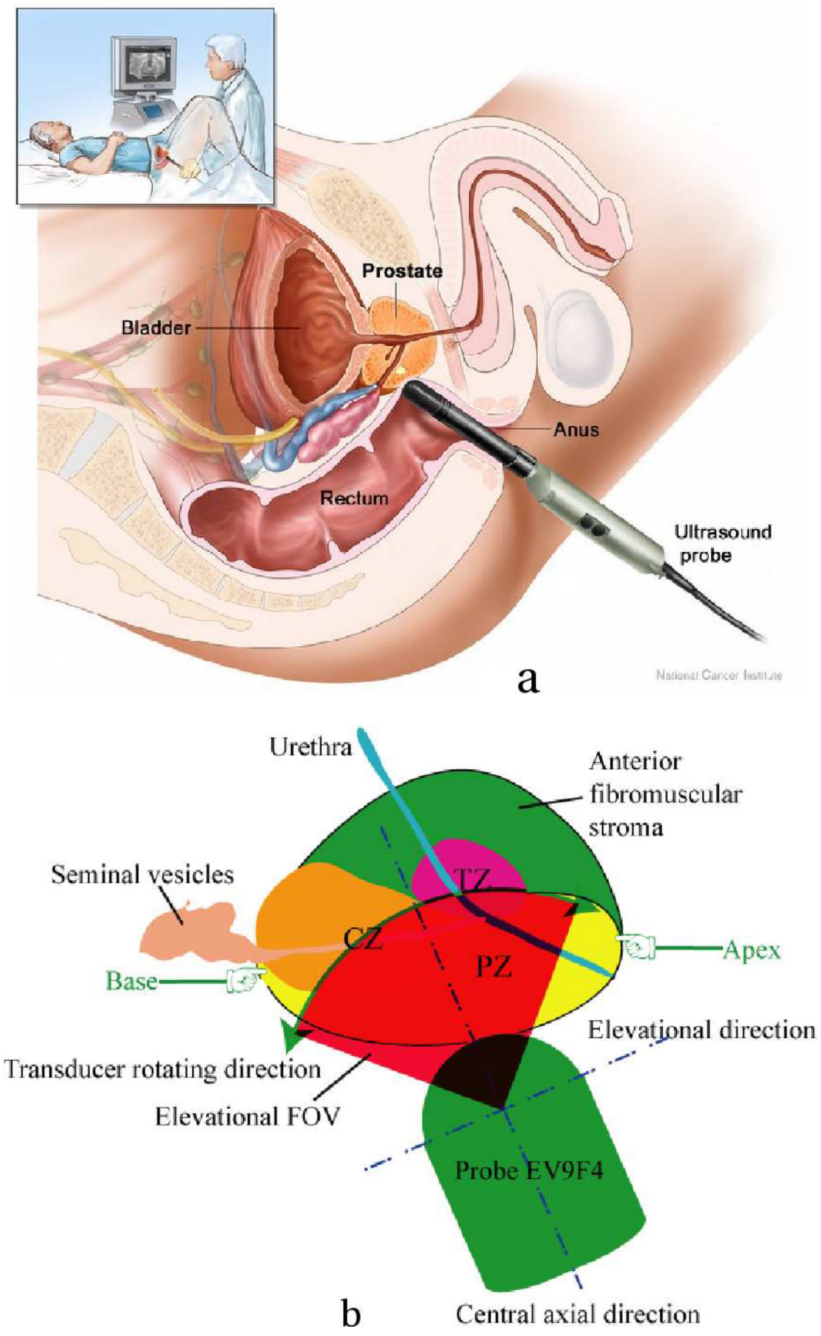

Figure 1.

Diagrams of ARFI prostate imaging *in vivo*. Both diagrams are in sagittal views, which are perpendicular to the imaging plane. (a) Experimental setup of ARFI imaging (the picture is taken from the NCI website(http://www.cancer.gov/cancertopics/pdq/treatment/prostate)). (b) Diagram of relative positions between the prostate and the imaging probe, and the elevational field of view (FOV, red filled area) of ARFI prostate imaging *in vivo*. The zonal structures, central zone (CZ), peripheral zone (PZ) and transitional zone (TZ) are labeled. To acquire 3D data, the ultrasound transducer rotates inside the probe along the direction pointed by the green arrows, whose angular range is 90°.

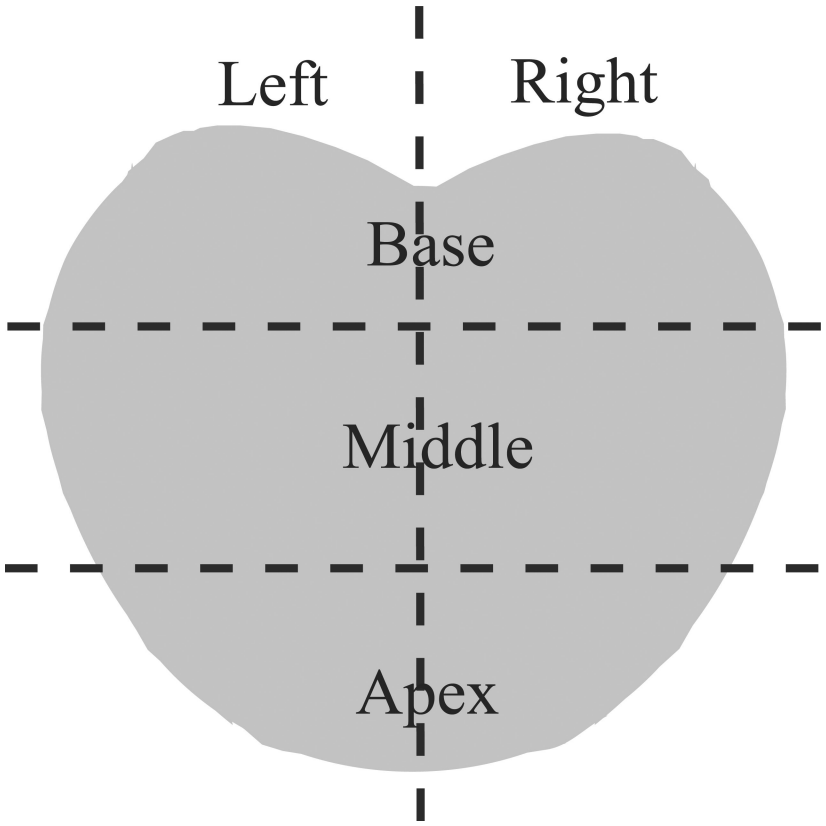

Figure 2.
Divisions of the prostate in a coronal plane.

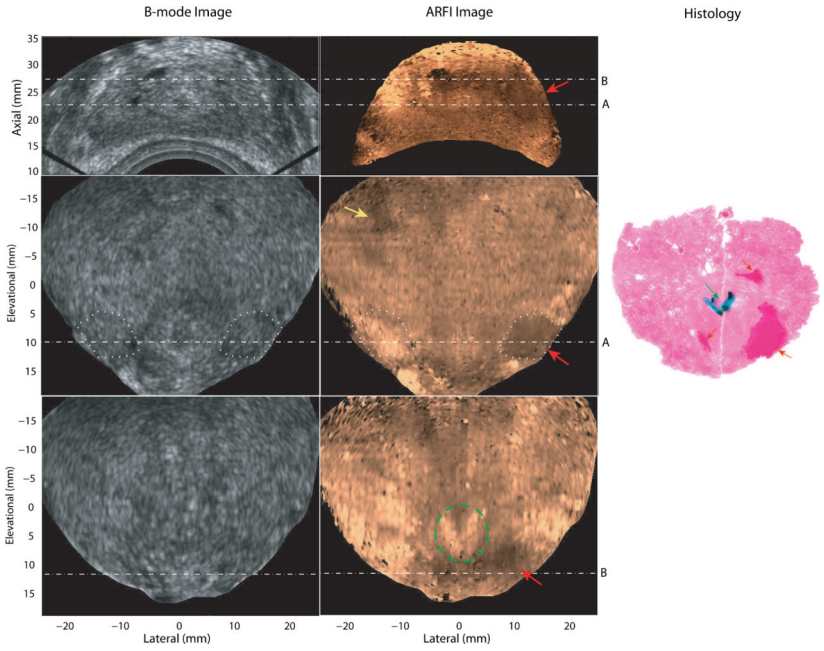

Figure 3.

Matched B-mode, ARFI and histological prostate images of Patient A. The first row shows an axial view (regular imaging plane) of the prostate; the second and third rows are two parallel coronal views. The axial imaging plane intersects the two coronal planes at the dashed lines, A and B, with an angle of 64°. In ARFI images, confirmed regions of PCa are indicated by red arrows; a suspicious cancerous region not confirmed by histological data is indicated by a yellow arrow; and the two ejaculatory ducts and verumontanum are circled with green lines. The regions circled with white dotted lines were used to compute CNRs of the PCa in the B-mode and ARFI images. In the histological slide, the cancerous regions (Gleason's core 4+3) are masked in red and indicated by red arrows; the ejaculatory ducts and verumontanum are masked in dark green with a green arrow. Small PCa foci (less than 1 mm) are circled with white dashed lines.

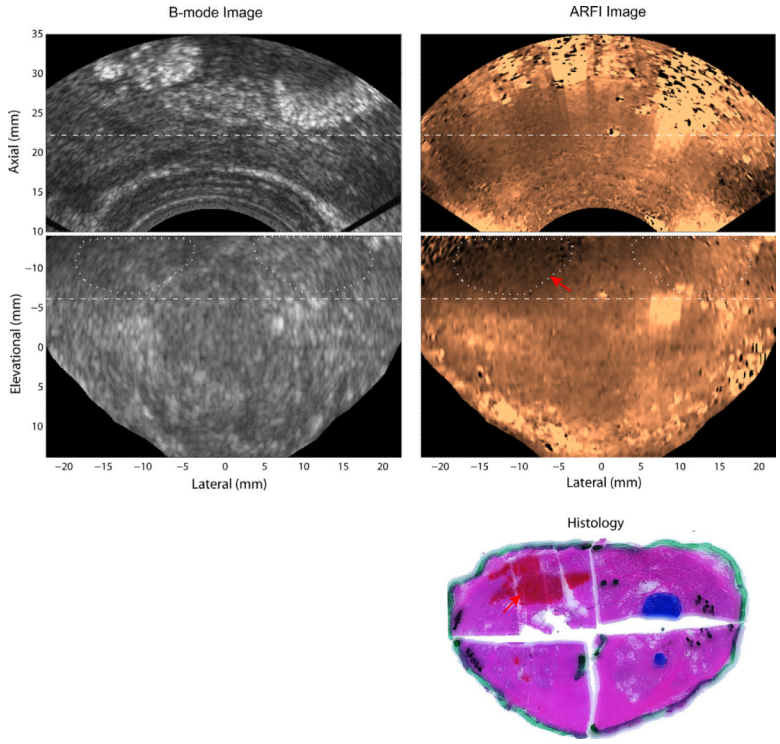

Figure 4.

Matched B-mode, ARFI and histological prostate images from Patient B. The top two rows are axial and coronal images, respectively. The two imaging planes intersect at the dashed lines with an angle of 74°. In the coronal ARFI image, the asymmetric stiff region indicated by the red arrow corresponds to the PCa (area masked in red) identified in the reconstructed whole-mount histological image (third row). The Gleason's score of this PCa is 3+3. The regions circled with white dotted lines were used to compute CNRs of the PCa in the B-mode and ARFI images.

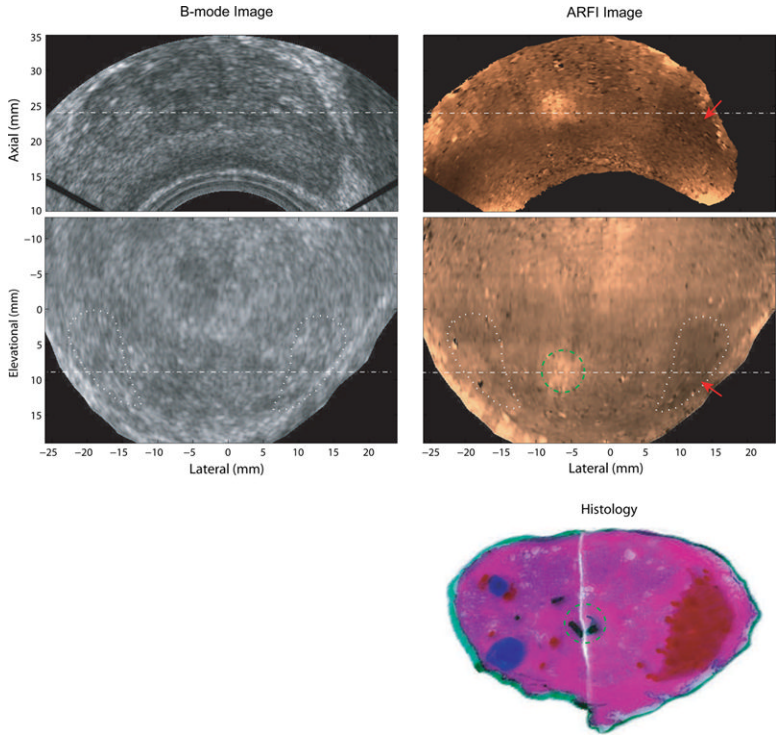

Figure 5.

Matched B-mode, ARFI and histological prostate images of Patient C. The top row shows axial B-mode and ARFI images. The middle row shows the coronal images. The two imaging planes intersect at the dashed lines with an angle of 20°. PCa is indicated by red arrows in ARFI images and marked red in the reconstructed whole-mount histological image. The two ejaculatory ducts are circled with green dashed lines. BPH nodules are masked in blue. The Gleason's score of this PCa is 3+4. The regions in the coronal view circled with white dotted lines were used to compute CNRs of the PCa in the B-mode and ARFI images.

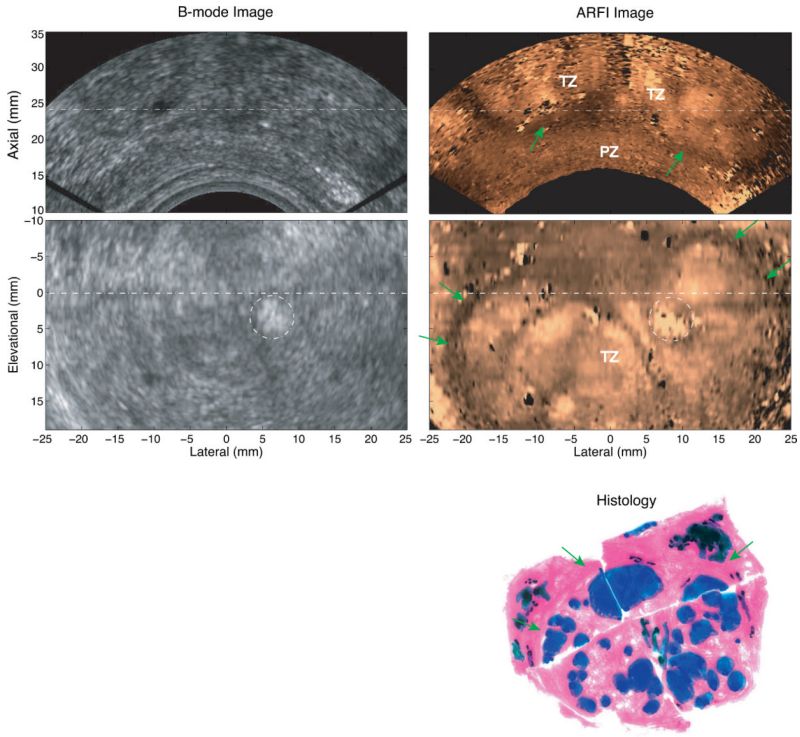

Figure 6.

Matched B-mode, ARFI images and a histological prostate image from Patient D. The top row shows axial B-mode and ARFI images. The middle row shows the coronal images. The two imaging planes are orthogonal to each other and intersect at the dashed lines. The green arrows indicate the boundary of the TZ. The hyperechoic region circled in the B-mode image is calcification. Complicated BPH nodules were identified (colored in blue) in the histological image.

Table 1

ARFI parameters for imaging human prostates *in vivo*

	Excitation beam	Tracking beam*
Center frequency (MHz)	4.0	8.9
Lateral F/#	2.9	1.0
Focal depth (mm)	20	20
Pulse length duration	100 μs	1–2 cycles
$I_{sppa.7}$ (W/cm^2)	1,675	-
Angular push spacing2	2.20°	0.55°
Number of pushes/plane	55	-
Parallel-receive beams	-	4
Pulse repetition frequency (PRF, kHz)	-	9.5

3D data acquisition settings	
Angular spacing between planes	1.8°
Number of 2D planes	50
Angular range	[−45°, 45°]
Acquisition time	3 min

*The tracking beams are standard B-mode beams.

Table 2

PCa findings of ARFI prostate imaging *in vivo*

	Number of patients
Sequence test	1
Noisy data	3
ARFI-histology registration not achieved	5
Confirmed PCa in ARFI images	7
Only PCa less than 2 mm identified by histology	3
Total	19

Table 3

Summary of all confirmed PCas

Lesion ID	Gleason's Score	Lesion size (x,y,z (mm))		Contra-lateral CNR		SR
		Histology	ARFI	ARFI	B-mode	
A1	3+4	4×7	4×5×6	2.2	1.1	1.6
B1	3+4	11×8	12×10×14	2.8	0.4	1.9
B2	3+3	4×3	5×4×6	1.4	1.4	1.6
C1	3+4	10×9	12×10×5	1.2	0.1	1.4
D1	3+4	10×14	8×6×5	1.3	0.6	1.2
D2	3+3	7×6	5×8×5	1.4	1.3	1.5
E1	3+4	10×8	15×8×7	2.9	1.2	1.5
F1	3+4	7×11	8×13×7	1.9	0.4	1.6
G1	3+3	9×7	7×14×6	3.9	2.4	2.1